

Article

Cold Spraying of Thick Biomimetic and Stoichiometric Apatite Coatings for Orthopaedic Implants

Ambra Paterlini ^{1,*}, Joël Alexis ² , Yannick Balcaen ² and Ghislaine Bertrand ¹

¹ CIRIMAT, Université de Toulouse, CNRS, INP-ENSIACET, 4 Allée Emile Monso, BP44362, CEDEX 4, 31030 Toulouse, France; ghislaine.bertrand@ensiacet.fr

² Laboratoire Génie de Production, INP ENIT, 47 Avenue d'Azereix, 65000 Tarbes, France; joel.alexis@enit.fr (J.A.); yannick.balcaen@enit.fr (Y.B.)

* Correspondence: ambra.paterlini@3deusdynamics.com

Abstract: Ceramic coatings have a long history in the orthopaedic field, with plasma sprayed coatings of hydroxyapatite as leading standard in the manufacturing process; however, these coatings can contain secondary phases resulting from the decomposition of hydroxyapatite at high temperatures, which limit the lifetime of implants and their osseointegration. This work aims to produce coatings that can maximize bone osseointegration of metallic implants. In order to preserve the raw characteristics of hydroxyapatite powders that are thermally unstable, coatings were deposited by cold spray onto Ti6Al4V alloy substrates. In contrast with other thermal spray technologies, this process presents the advantage of spraying particles through a supersonic gas jet at a low temperature. On top of hydroxyapatite, carbonated nanocrystalline apatite was synthesized and sprayed. This biomimetic apatite is similar to bone minerals due to the presence of carbonates and its poor crystallinity. FTIR and XRD analyses proved that the biomimetic characteristics and the non-stoichiometric of the apatite were preserved in the cold spray coatings. The cold spray process did not affect the chemistry of the raw material. The adhesion of the coatings as well as their thicknesses were evaluated, showing values comparable to conventional process. Cold spraying appears as a promising method to preserve the characteristics of calcium phosphate ceramics and to produce coatings that offer potentially improved osseointegration.

Keywords: cold spray; biomimetic apatite; hydroxyapatite; Ti6Al4V implants



Citation: Paterlini, A.; Alexis, J.; Balcaen, Y.; Bertrand, G. Cold Spraying of Thick Biomimetic and Stoichiometric Apatite Coatings for Orthopaedic Implants. *Coatings* **2022**, *12*, 722. <https://doi.org/10.3390/coatings12060722>

Academic Editor: Mohammadreza Daroonparvar

Received: 29 April 2022

Accepted: 21 May 2022

Published: 24 May 2022

Publisher's Note: MDPI stays neutral with regard to jurisdictional claims in published maps and institutional affiliations.



Copyright: © 2022 by the authors. Licensee MDPI, Basel, Switzerland. This article is an open access article distributed under the terms and conditions of the Creative Commons Attribution (CC BY) license (<https://creativecommons.org/licenses/by/4.0/>).

1. Introduction

Bone fractures and pathologies are important areas of study, especially as osteoporosis and osteoarthritis cases have steadily increased in recent decades. Worldwide, osteoporosis causes more than 8.9 million fractures per year—resulting in one osteoporotic fracture every three seconds—and half of the world's population aged 65 years or older suffers from osteoarthritis [1,2]. Demographic growth and the ageing of people are major drivers of this steady increase, which is also impacted by accidents and the lack of sustained physical activities. According to a survey including 17 countries with a total population of 742 million people, total knee primary and revision surgeries alone are estimated at 1,183,000 per year: an average rate of 159 surgeries/100,000 people [3]. The replacement, repair, and restoration of defective bearing joints, teeth, or spines require an implantable medical device to help the patient quickly regain autonomy and mobility in a sustainable way. Implants must provide both mechanical functions (mechanical stress, wear, fatigue) and the continuity of biological functions (cell growth, tissue formation) over the long-term. In order to guarantee the mechanical resistance, metallic alloys are commonly selected for orthopaedic implants. To improve their biological properties and the corrosion resistance, bioactive coatings have been introduced on these implants since the mid-1980s. Several methods have been investigated, mainly concerning the thermal spraying of biocompatible materials, but also the electrochemical deposition, chemical vapor deposition, and

dip coating [4–6]. The main limits of the latter two are the low thickness achieved and the limited mechanical properties [7,8]; therefore, the prevailing method to coat metallic orthopaedic implants remains to be the plasma spraying of stoichiometric hydroxyapatite, commonly known as hydroxyapatite ($\text{HA—Ca}_{10}(\text{PO}_4)_6(\text{OH})_2$). Even though plasma spray HA is very effective as a bioactive coating, several cases of failure still occur due to fractures, infections, or the aseptic loosening of implants caused by fatigue due to repeated mechanical stress or poor ingrowth due to improper fit at the bone interface [9–11]. These failures have been attributed to the partial thermal degradation of hydroxyapatite by the plasma process leading to calcium phosphate phases that exhibit different dissolution rates; therefore, some authors have defined the ideal bio-properties required for a coating: biocompatibility, osteoinduction (recruitment and stimulation of stem cells to develop pre-osteoblasts), osteoconduction (promotion of osteoblasts), mechanical stability, and antimicrobial properties [12,13]. The materials that can match these properties are the calcium phosphate nanocrystalline apatites—the ones that are major constituents of bones. Over recent decades, various studies focused on the ways to synthesize those biomimetic apatites [14–17]. This synthetic biomimetic apatite is composed of nanosized crystals covered by a calcium phosphate non-apatitic hydrated layer containing labile ionic species [18,19]. This highly reactive biomimetic apatite is thermally sensitive. This is the reason why plasma spray is not suitable for implementing biomimetic apatite materials. Various wet processes have been explored to deposit a biomimetic apatite coating [20,21]. Unfortunately, there are still no commercially available processes to produce hydroxyapatite as well as biomimetic apatite [13,14].

To cope with this challenge, the idea was to implement cold spray (CS) to produce biomimetic calcium phosphate coatings. CS is a coating deposition method based on the acceleration of solid particles by a supersonic gas jet (up to 1200 m/s) towards a substrate. Upon impact, powder grains split on the surface and they spread and stack due to plastic deformation to generate the coating; therefore, this technology is particularly suitable for plastically deformable materials (such as metals) [22–24]. In the literature, metal-ceramic mixtures (cermet) have already been tested to produce cold sprayed coatings [25–28], but few works concern pure ceramics [29,30]. The adhesion of the coating to the substrate is quite challenging, and due to their general fully elastic behaviour, the physical phenomena allowing ceramic coating formation are still uncertain. Some recent studies have demonstrated that the properties of powders and substrates have a strong influence on the feasibility of the coating, its cohesion, and its adhesion [31–34]. In particular, the powder must present an excellent flowability to avoid feed rate fluctuations and inhomogeneous deposits—particle shape and size distribution are thus major characteristics [32,35–37]. Regarding the substrate, the most impactful property seems to be hardness; hard substrates facilitate granular fractures by improving coating cohesion and deposition rate, whereas for softer substrates, adhesion prevails [33,38]. One of the main advantages of cold spraying, besides the reduced cost and energy consumption, is related to the low operating temperature—which significantly reduces most of the risks associated with common thermal processes used to coat implants, such as plasma spraying. Indeed, the high temperatures that characterize plasma spraying can generate secondary phases, such as: calcium oxide (CaO) resulting from the volatilization of phosphorous; α -tricalcium phosphate (α -TCP); and tetracalcium phosphate (TTCP), which occurs due to the thermal decomposition of HA above 1500 °C. β -tricalcium phosphate occurs due to the cooling transition of α -TCP at 1000–850 °C [39]. All these phases can affect the coating homogeneity, its dissolution behaviour, and its adherence to bone. The lower temperatures characterizing CS guarantee the absence of deleterious evaporation phenomena, residual stresses or phase alteration [40–42].

The objective of this study was to validate the feasibility of producing stoichiometric hydroxyapatite and biomimetic apatite coatings by cold spraying, in order to maximize the adherence at the implant-bone interface and to reduce the integration time of the prosthesis. The main goal is to achieve thick and highly adhesive coatings in order to guarantee

suitable performances for orthopaedic implants. Different powders were tested: two types of commercial stoichiometric hydroxyapatite, produced by different processes, and a carbonated Biomimetic Nanocrystalline Apatite (BNAc) synthesized in the laboratory. All the coatings were deposited on grade 5 titanium alloy (Ti6Al4V) plates, the most common alloy used for biomedical implants. Different surface pre-treatments were implemented and adjusted to the sprayed material. The microstructural characterizations of the cold sprayed coatings, as well as the thickness values achieved, were related to the raw powder properties, flowability, and particle size distribution. Furthermore, a mechanical analysis allowed for the evaluation of the adherence of the deposited coatings.

2. Materials and Methods

2.1. Feedstock Materials

The two commercial powders used in this study were both made of fully crystalline stoichiometric hydroxyapatite, produced by two different processes. The first, supplied by Teknimed SA—France, was sintered and crushed (SC), whereas the second, supplied by Medicoat AG—Switzerland, was spray dried and sintered, resulting in spherical agglomerates (AA). Their purity and crystallinity were verified by X-ray diffraction, whereas their stoichiometric ratio (Ca/P = 1.67) was verified by ICP chemical dosing. The BNAc was produced following the synthesis protocol that was developed and described by Cazalbou et al. [18].

The synthesis was obtained by precipitation into a pilot reactor involving two separated solutions, R1 and R2, whose compositions are listed in Table 1. Once all solid components are fully dissolved in R1 and R2, R1 is rapidly poured into R2, resulting in the following reaction:



After 24 h of maturation, the solution is filtered through Büchner funnels, washed with deionized water and finally lyophilized during 72 h.

Table 1. Biomimetic apatite powder synthesis procedure.

Solutions	R1—Calcium Source	R2—Phosphates and Carbonate Source
Solid components	261 g Ca(NO ₃) ₂ 4H ₂ O	360 g (NH ₄) ₂ HPO ₄ 360 g NaHCO ₃
Deionised H ₂ O	3750 g	13,500 g

The resulting BNAc powders were ground and sieved to obtain batches of different size distributions.

Powder densities of SC, AA, and BNAc (before grinding) corresponds to 0.87, 0.54, and 0.19 g/cm³, respectively [5,43]. Powder acronyms and their main properties are listed in Table 2.

Table 2. Powders used for cold spray coatings, acronyms and main properties.

Acronym	Material	Preparation	Density
SC	Hydroxyapatite	Sintered and crushed	0.87 g/cm ³
AA	Hydroxyapatite	Spray dried agglomerates	0.54 g/cm ³
BNAc	Nanocrystalline apatite	Synthesized and crushed	0.19 g/cm ³

Laser-cut titanium alloy rectangular plates (55 × 75 × 1.6 mm) were used as substrates for the coatings. The alpha-beta titanium alloy Ti-6Al-4V—grade 5 was selected as the sub-

strate material for its sufficient mechanical strength and corrosion resistance; its chemical composition is illustrated in Table 3.

Table 3. Chemical composition of Ti6Al4V—Grade 5 alloy (wt.%).

Element	Aluminium	Vanadium	Iron	Oxygen	Hydrogen	Titanium
wt.%	6	4	<0.25	<0.2	<0.015	Balance

2.2. Cold Spray

Coating deposition was produced at the *Thermal Spray Centre (CPT)* in Barcelona—Spain, using a low-pressure cold spray system, Dymet 423, using a de Laval nozzle. Air was used as a carrier gas to accelerate powders stored into a vibrating feeder, and heated to temperatures in the range of 100–500 °C. Gas pressure was maintained between 0.5 and 0.8 Mpa, corresponding to powder feed rates in the range of 3.5–4.7 g/min. The main spray parameters consisted of: a constant spray distance of 15 mm maintained for all coatings; a vertical step from 0.75 to 3 mm; and a scanning speed varied between 10 and 50 mm/s.

Two different types of sample preparation were tested on Ti6Al4V substrates: alumina sand-blasting at 250 mm/s scanning speed (air temperature varying from 25 to 200 °C) carried out with the same cold spray, and pre-coating with a plasma sprayed HA produced by 2PS—*Projection Plasma Système* company (Montbazens—France). Plasma spray underlayers were obtained using Ar-H₂ plasma, with a 100 mm spray distance and a power of 30 kW.

2.3. Powder and Coatings Characterization

The powder particle size was measured using a MALVERN Mastersizer 3000 laser-based particle size analyser (Malvern Panalytical, Palaiseau, France), using the AERO S module under dry conditions. The powder was injected into the scanning area with a pressure of 0.1 Mpa after passing through a vibrating chute to break the agglomerates. The powders' flowability was evaluated according to European Pharmacopoeia standard 01/2008:20915: this method consists of pouring 50 g of powder into a graded cylinder that is regularly tapped. After 10 and 1250 taps, the volume is registered in order to determine the corresponding density values, ρ_{bulk} and ρ_{tapped} , respectively, that allows the calculation of the compressibility or Carr's Index (CI) [44], as shown in Equation (1):

$$\text{CI} = 100 \times ((\rho_{\text{tapped}} - \rho_{\text{bulk}}) / \rho_{\text{tapped}}) \quad (1)$$

The flow character is considered 'excellent' if the CI is lower or equal to 15% [45,46]. Various microstructural analyses were performed on the powders and coatings for comparison: X-Ray Diffraction (XRD); Fourier Transform Infrared (FTIR) spectroscopy; and Scanning Electron Microscopy (SEM). The crystalline phases were identified by a BRUKER D8 GIXRD diffractometer (Bruker France, Champs-sur-Marne, France), equipped with a Cu anode ($K\alpha = 1.5418 \text{ \AA}$). Diffractograms were recorded in a 2θ range between 20–80°, with a step size of 0.02°, and an integration time of 5 s. The full-width at half-maximum (FWHM) was extracted from XRD data after the diffractogram fitting. The Scherrer equation [47] (Equation (2)) was used for an estimation of the crystallite size (D) for BNAC:

$$D = 0.94\lambda / \beta \cos\theta \quad (2)$$

where λ represents the wavelength of Cu K(α), β is the peak FWHM, and θ is the angle of the peak in degrees. Peaks at $2\theta \approx 25^\circ$ and $2\theta \approx 40^\circ$ were selected, corresponding to (002) and (310) crystallographic planes, in order to avoid peaks overlapping.

FTIR spectroscopy allowed the investigation of chemical bonds and functional groups using a Nicolet 5700 Thermo spectrometer (Thermo Scientific, Paris, France), providing spectra in the far-infrared region (400–4000 cm^{-1}) by transmission mode with a 4 cm^{-1} resolution. Samples were prepared by dispersing powders and scratched coatings in dried potassium bromide pellets. Previously reported data [10] served as starting point for the

positioning of each contributing band existing in this spectral domain: at 470 cm^{-1} corresponding to $\nu_2(\text{PO}_4^{3-})$; $530\text{--}534\text{ cm}^{-1}$ (non-apatitic HPO_4^{2-}); 550 cm^{-1} (apatitic HPO_4^{2-}); $560/575\text{ cm}^{-1}/601\text{ cm}^{-1}$ (apatitic PO_4^{3-}); 617 cm^{-1} (non-apatitic PO_4^{3-}); 631 cm^{-1} ($\nu_L(\text{OH}^-)$); and 670 cm^{-1} (H_2O libration mode).

The powders and coatings of the microstructures were analysed using a FEI Quanta 450 SEM (FEI Europe, Eindhoven, Netherlands) at low vacuum mode (chamber pressure between 80 and 100 Pa). The electron beam current intensity was maintained in the range of 0.04–0.1 nA and the high voltage was maintained between 10 and 12 kV. Energy Dispersive X-ray spectroscopy (EDX) analyses were performed using a high vacuum (pressure $< 10^{-3}$ Pa), elemental maps were acquired with voltage in the range of 5–15 kV and a current intensity in the range of 4–6 nA. The thickness and the porosity of the coatings were analysed by image analysis using the software ImageJ. For the coating thickness, optical microscope (Nikon Eclipse MA200) images were used, and 3 thickness values were measured on 4–5 images to obtain an average value. For the coating porosity, SEM binary images were analysed using the *Analyse Particles* tool to measure all pore areas and the corresponding coating porosity (%). At least 3 images for each coating were analysed.

Mechanical tests were carried out to evaluate the coating adherence. The three-point bending test was performed in accordance with the ISO 14 679 standard. For this test, a stiffener is glued to the coating and the sample is loaded on the opposite side. The drop on the load vs. displacement curve (Figure 1-1) indicates the value of the critical load—it corresponds to the initiation of the detachment of the coating from the support. Then, the failure occurs, and finally, the third part of the curve (Figure 1-2) represents only the mechanical response of the substrate and is therefore not taken into account. The stiffener is cast using a mixture of AW134 resin and HY997 hardener, cured over 8 h. After the test, the stiffener is completely removed and the failure modes are analysed using SEM and EDX analysis to determine fractions of adhesive or cohesive failure.

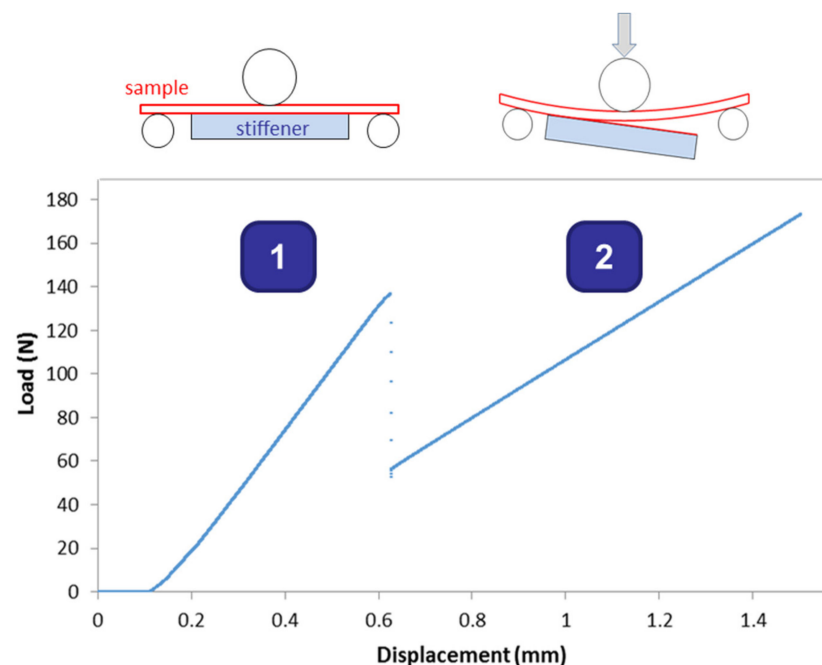


Figure 1. Bending test curve—coating critical load determination.

3. Results

3.1. Powders Characterization

Figure 2 presents the particle size distribution of the four powders used to produce CS coatings and the corresponding volume distribution coefficients of $Dv(10)$, $Dv(50)$, and $Dv(90)$. BNAC and SC powders exhibit a rather monomodal volume-based particle size

distribution centred at 76 μm and 149 μm , respectively. In contrast, ground BNAc and AA powders have a multimodal particle size distribution. There is also a significant difference between the median particle size of the two commercially available powders; the Dv50 corresponds to 59.3 μm for the AA powder and 149 μm for the sintered one. In addition, the effect of the grinding treatment is highlighted: the median particle size value of the BNAc powder changes from 76.3 μm to 22.8 μm with milling. Powders were also analysed in terms of flowability, directly linked to their compressibility by the Carr Index. The resulting CI values are: $11.5\% \pm 0.9$ for BNAc, $19.9\% \pm 1.3$ for ground BNAc, $13\% \pm 0.5$ for SC, and $10.1\% \pm 0.3$ for AA, which means that the flowability is classified as ‘excellent’ for all powders except for the ground BNAc that is only ‘good’. SEM images (Figures 3 and 4) show the microstructures of the powders. The sintered–crushed powder and the BNAc powder have similar irregular angular faceted shapes due to their manufacturing processes; conversely, the AA powder results in smaller powder grains with a regular spherical shape. Polished cross-sections of the particles were also observed by SEM: AA powders have a porous core, whereas BNAc and SC are fully dense and homogenous.

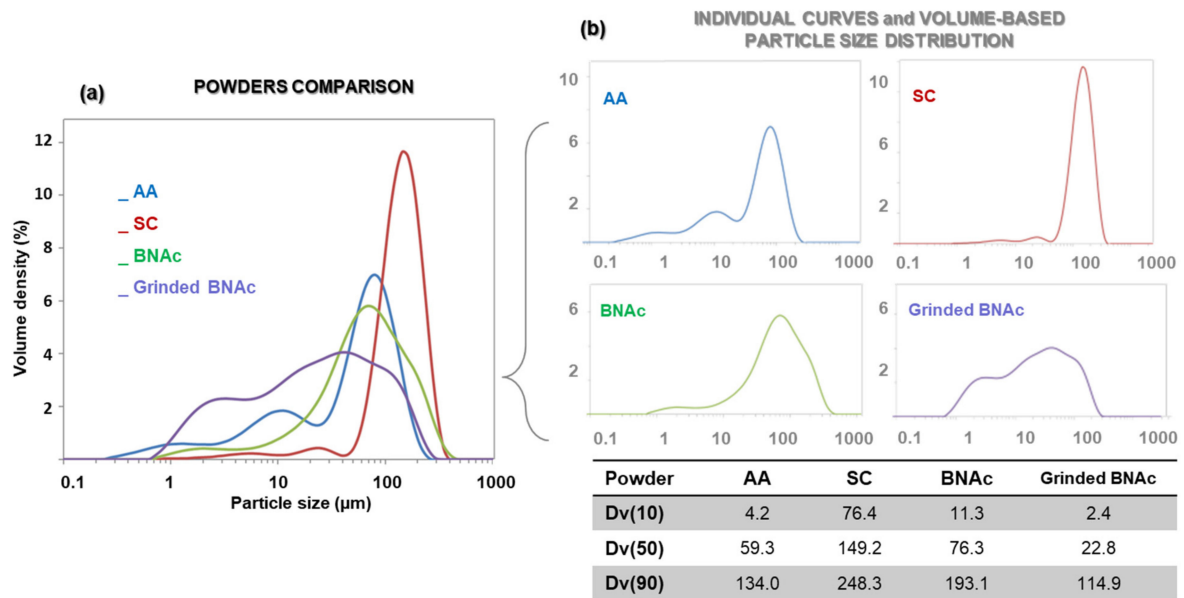


Figure 2. Particle size distribution of AA, SC, BNAc, and ground BNAc powders: (a) general comparison, and (b) individual curves and volume-based distribution coefficients.

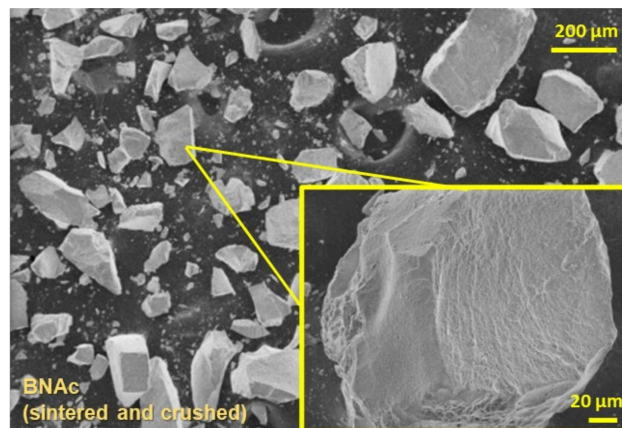


Figure 3. BNAc powder SEM analysis.

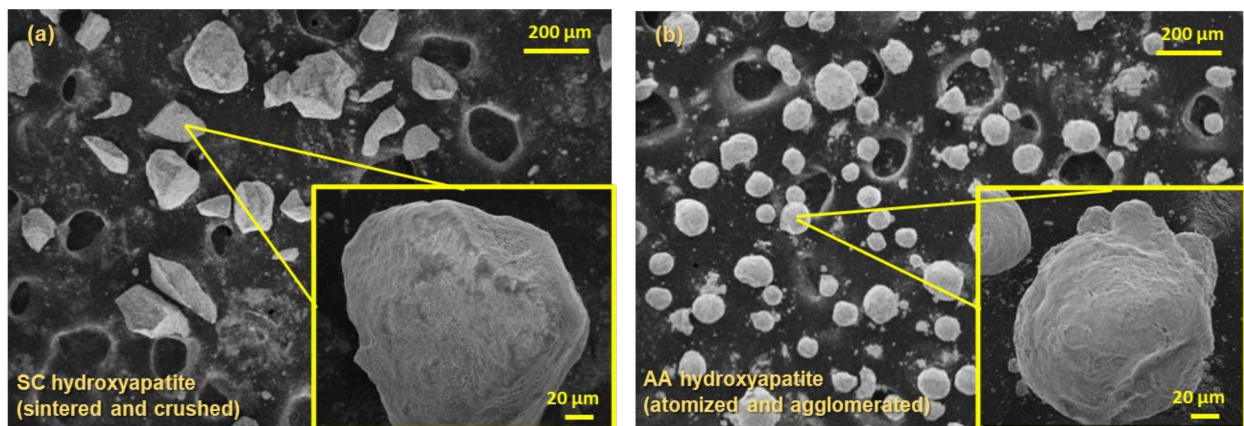


Figure 4. Commercial powders SEM analysis: (a) SC powders and (b) AA powders.

3.2. Powder-Coating Comparison

XRD and FTIR analyses allow for the comparison of the materials before and after cold spray. As expected, X-ray patterns presented in Figure 5 show the very high crystallinity of both commercial powders (given by the sharp X-ray peaks) and the poorly crystallized structure of the BNAc powder (given by the broad scattering profile). The BNAc powder and coating nano-crystallinity were verified through the Scherrer calculation of crystal size (D). In the case of BNAc powders, D values of 7.6 nm and 6.2 nm were found for the (002) and (310) crystallographic plans, respectively. For BNAc coatings, the crystal sizes for the same plans measured 6.9 nm and 5.4 nm. For the three samples, all the peaks match with those of hydroxyapatite (JCPDS reference n. 09-432 [18]) and no secondary phase is detected. The diffractograms of the three powders correspond well with the corresponding coatings, which indicates that the deposition process does not transform the crystalline structure and features of the raw powders.

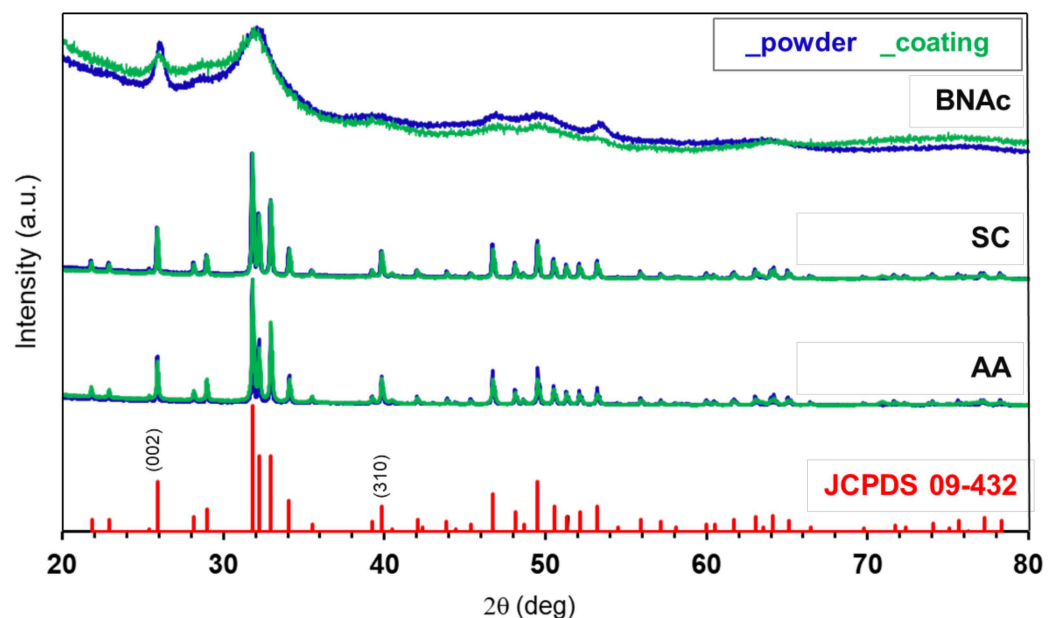


Figure 5. XRD analysis: comparison between powders and coatings composition.

FTIR analysis (Figure 6) confirms this result: there is a strong agreement between the spectra of the calcium phosphates before and after deposition. The main infrared absorption bands characterizing apatite (OH^- , PO_4^{3-} and HPO_4^{2-}) can be identified in all spectra in the $400\text{--}800\text{ cm}^{-1}$ wavenumber range corresponding to the $\nu_2\nu_4$ (PO_4) and ν_L (OH) vibration modes of phosphate and hydroxide ions. The band at $1550\text{--}1350\text{ cm}^{-1}$ range

corresponds with the ν_3 vibrations of the carbonates (CO_3^{2-}) contained in the biomimetic apatite. These bands are centred at $\approx 1410 \text{ cm}^{-1}$ and $\approx 1460 \text{ cm}^{-1}$, meaning that carbonates substitute at the phosphate (PO_4^{3-}) sites, thus defining a B-type apatite (the presence of a band centred at $\approx 1530 \text{ cm}^{-1}$ would have indicated the presence of an A-type apatite, where carbonates substitute at the hydroxide sites) [48].

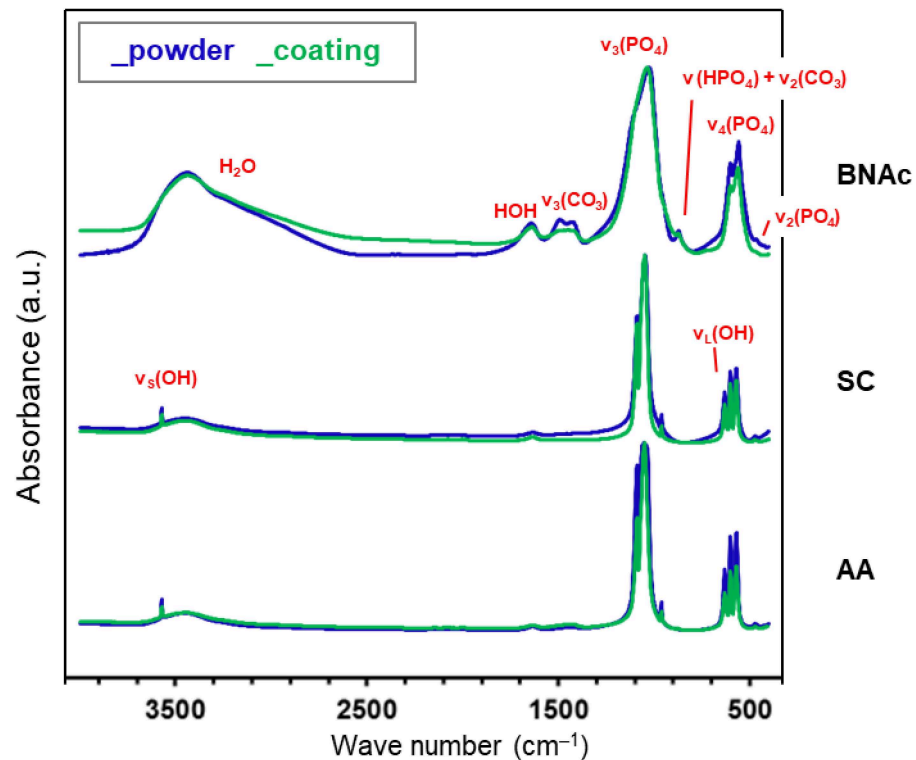


Figure 6. FTIR analysis: comparison between the powder and coating compositions.

3.3. Coating Microstructure and Adhesion

A series of experiments were performed in order to define the pre-treatments favouring the deposition of a coating made from one of the selected powders. To produce a coating from the BNAc powder, an underlayer is required. The best result was achieved using a plasma sprayed HA layer. To produce a coating from a commercially available powder (SC or AA powders), the sandblasting step was carried out using alumina powder with adjusted particle size distribution and the cold spray device. The microstructures of the coatings were observed by SEM. The polished cross-section images are presented in Figures 7 and 8. The coating made with the BNAc powder (Figure 7) shows a heterogeneous thickness distribution varying from $60 \mu\text{m}$ to $120 \mu\text{m}$. Its interface with the HA plasma sprayed coating is continuous and free of cracks or defects. On the other hand, the thickness of the HA coatings is quite homogeneous, around $35 \mu\text{m}$, for a coating made from SC powder, and $20 \mu\text{m}$, for the one produced with the AA powder. Thickness data are reported in Figure 9, the heterogeneity of biomimetic apatite coatings is confirmed by the high errors on its thickness value. AA and SC are 25–30% thinner compared with the BNAc layer. BNAc presents the lowest density, with a $40 \pm 4\%$ porosity, whereas SC and AA values correspond to $28 \pm 5\%$ and $28 \pm 4\%$ porosities, respectively.

Some cracks are detectable (especially for AA powder-based coating), and residual corundum grains or roughness due to sandblasting can generate defects at the interface. Furthermore, especially for these later coatings, the nanoparticles that are easily identified in the SEM images indicate that the initial powders are broken down into smaller particles. To establish when this breakage occurs, a spray test was carried out by directing the powder jet into a bin full of water (to soften the impact force). The powders were observed and

their particle size was measured after being recovered. They retain the same shape and dimension after testing—this means that the powder breakage is not due to the applied gas pressure in the spray system, but it occurs once the particles hit the solid substrate, upon impact.

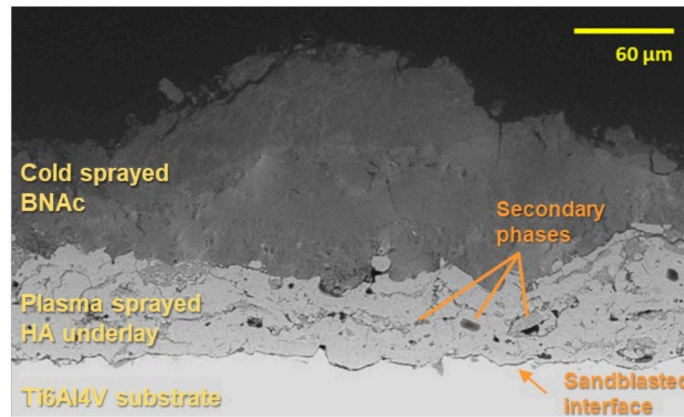


Figure 7. BNac coating on plasma sprayed HA underlay at SEM.

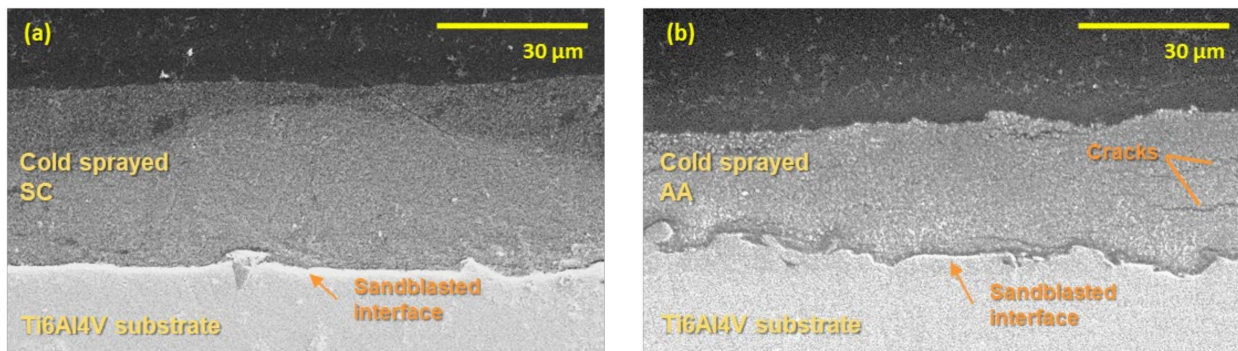


Figure 8. Commercial HA coatings SEM analysis: (a) SC coating and (b) AA coating.

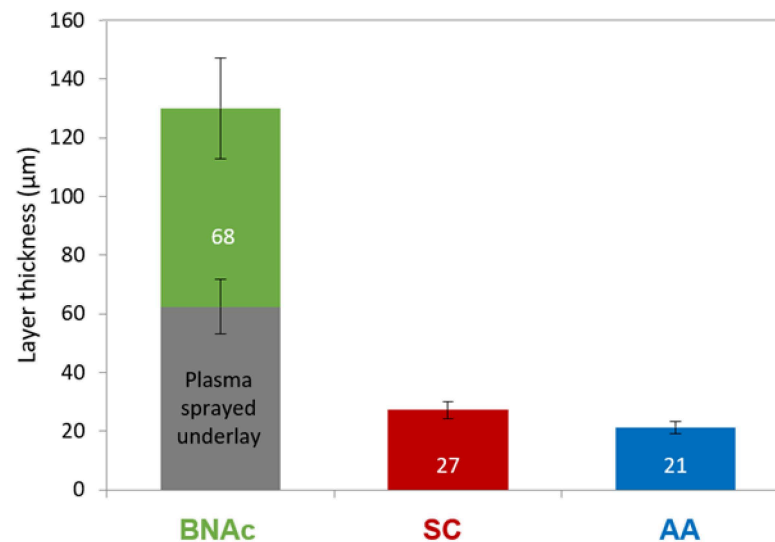


Figure 9. Coating thickness.

Bending tests not only provide a critical load, which characterizes the coating adherence, but they allow a comparison between different types of rupture. The data in Figure 10 provides evidence of a higher apparent adhesion for the SC powder-based coating, the failure of which occurs at a force of 69 N, whereas for the AA and BNac powder-based

coatings, the critical load is only 10% of that measured for the standard plasma sprayed coating (used as reference). Using EDX mapping on the fracture surface, three different propagation modes were detected: adhesive, cohesive, and mixed (Figure 11). Table 4 reports the element analysis of the post-mortems of the tested areas—the main elements which correspond to substrates are Ti and Al, while the elements representing the coatings are Ca and P. To assess the unstable crack propagation mode, a quantification of the Ca element in the post-mortem surface in EDX analysis was used. With less than 30% of the surface covered by Ca, the propagation is assumed to be adhesive, as over 70% of the remaining surface covered by the HA coating corresponds to a cohesive propagation mode, and the range between 30% and 70% corresponds to a mixed mode. A mixed failure propagation mode is found for the SC powder-based coating with 32% of the post-mortem tested area covered by HA, whereas a cohesive failure was evidenced for both AA and BNAC powder-based coatings, where only 7% and 1% of the coating was left on the surface after the test, respectively. An adhesive fracture was used for the plasma spray reference sample, with 80% of the coating removed during the test. The example of mixed failure propagation EDX mapping on the SC coating is reported in Figure 11, along with the scheme of failure modes (on the left). The lower part of mapping images corresponds to the imprint of the stiffener after breaking, and the upper part is the surrounding untested coated area. The presence of calcium and phosphorus on the area covered by the stiffener corresponds to the fraction of the coating that remains attached to the support; however, the presence of titanium, aluminium, and vanadium in the same area permits it to be distinguished from a mixed propagation that involves the interface.

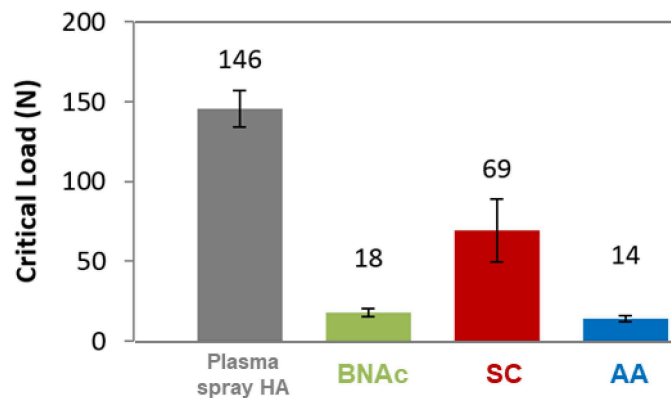


Figure 10. Bending test coating critical load.

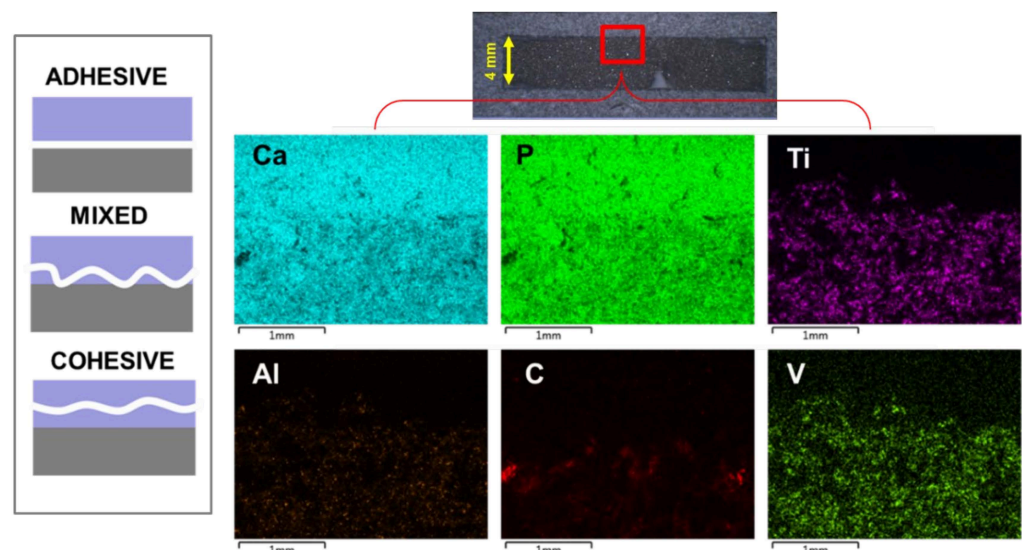


Figure 11. Breaking types and an example of SC coating mixed rupture by EDX mapping.

Table 4. EDX chemical analysis on adhesion tested parts in the centre of the breaking zone and estimation of coating loss.

Element (wt.%)	Plasma Spray Ref.	BNAc	AA	SC
O	29.66	41.08	40.07	39.27
Na	0.04	0.14	0.17	0.09
Mg	0.04	0.18	0.3	0.01
Al	10.56	0.14	0.47	2.62
P	3.4	16.49	17.3	13.91
Ca	7.44	41.08	39.59	29.82
Ti	46.57	0.55	1.95	13.61
V	2.29	-	0.15	0.67
Si	-	0.33	-	-
Total	100	100	100	100
Est. coating loss	80%	7%	1%	32%

4. Discussion

4.1. Powders Characterization

The powder characterization comprised the first screening for the sprayable materials. According to state-of-the-art powder studies, the particle size significantly affects the flow character. Large particles (>250 μm) are normally free-flowing, whereas particles below 100 μm cause cohesion phenomena to occur, and for particle sizes around 10 μm , flow becomes almost impossible [49,50]. Furthermore, a narrow particle distribution promotes flowability [50,51]. Based on these considerations, the ground BNAc batch was discarded because of its large particle size distribution and its poor flowability—which was also confirmed by the compressibility index. The shape of the grain also plays an important role—spherical geometries are preferred to favour flowability [52]. This could explain the feasibility of AA powder-based coatings; despite the small dimensions of initial powders ($D_{v50} = 59 \mu\text{m}$), they present excellent flowability ($CI = 10.1\%$).

4.2. Powder-Coating Comparison

FTIR and XRD results confirm that the cold spray process is able to retain both the biomimetic and stoichiometric apatite compositions of the raw powders as no secondary phases were detected. As mentioned, up to now, the mechanism explaining the adhesion and cohesion of a ceramic coating made by cold spray is not fully established. Several studies associate it with the powders smashing and spreading, which, in a way, simulates the plastic behaviour of polymers and metals [32,33,38]. SEM analyses and the spray test in water confirm this hypothesis. Since there is no evidence of powder rupture prior to impact, but the coatings exhibit a nanoscale grain pattern, the formation of the coating must be linked to the crash of the powder against the substrate. Furthermore, as illustrated by Hanft et al. [52] and Winnicki [53], parameters comprise the kinetic energy, and particle size and their agglomeration state present a strong influence on the substrate impact. All powders analysed in this study are considered large particles (>10 μm), thus fragmentation is expected, as well as the abrasive blasting of the substrate (visible in the irregular interface between coating and the metallic plate); however, the lower hardness of HA and apatite could allow for the coating formation in conditions that are impossible for the most commonly analysed advanced ceramics (e.g., alumina and other oxide ceramics) [52,53].

4.3. Coating Microstructure and Powders Influence

The mechanical tests show different results for all the analysed cases, but there is no relation with the architectures of the coatings. In fact, the SC powder-based coating has a significantly higher critical load than the AA and BNAc powder-based ones, despite having a comparable thickness to AA and porosity in the same range. The mechanical resistance of the coating seems to be related to the type of failure. The SC powder-based coating is the only one to present a mixed propagation failure mode with a moderate

critical load, whereas it is cohesive for the AA and BNAC powder-based coatings with a very low critical load. A cohesive propagation failure corresponds to an adhesive force prevailing at the interface, which includes mechanical bonding, substrate roughness, and residual stresses. In contrast, the cohesive force is mainly determined by the sprayed material properties: microstructure, homogeneity, and crystallinity [54]. If a cohesive force prevails in the coating, the failure propagation is more likely to be mixed or adhesive. This means that there is a lack of coating cohesion in the AA and BNAC powder-based coatings (causing the observed cohesive failure), whereas for the SC powder-based coating, the cohesive force is higher, and this generates a mixed failure. For both SC and AA powder-based coatings, the surface preparation and roughness are the same, so this is not the reason for the different mechanical behaviour. Moreover, according to the literature, the adhesion should be increased for thinner coatings [54,55], but this is not the case for the SC and AA powder-based coatings (this latter is thinner and has poorer adhesion). Thus, coating thickness is not a key parameter either. The discriminating factor could be the characteristic of the powder (i.e., the low density of the AA and BNAC powders (for AA powder due to its porous core arising from the spray-dried process, for BNAC powder due to its microstructure) compared with the SC powder that can influence the coating formation). Various research has described how particle density affects a very important parameter for cold spray efficiency: the critical particle velocity. This parameter is specific for each material and is inversely related to the density of the powder [56–58]. Schmidt et al. determined a ‘window of deposition parameters’ depending on particle temperature and impact velocity for ductile materials [59], but this would be significantly limited if applied to ceramics, due to their poor thermal conductivity and their lack of ductility. Consequently, there would be a narrow range of possible velocities very close to the upper limit—also called ‘erosion velocity’—which, if exceeded, causes no adhesion of the particles and erosion of the substrate. The higher particle velocity of AA compared with SC (due to its lower density) can limit coating deposition and mechanical properties if too close to the erosion velocity, due to a high percentage of bouncing particles or low adhesion.

5. Conclusions

This study proved the feasibility of thick and adhesive cold spray coatings on grade 5 Ti6Al4V substrates using biomimetic and stoichiometric apatite powders without altering their composition. The low temperatures involved enabled the avoidance of the formation of secondary phases that could pollute coatings and reduce their mechanical and biological properties.

- The BNAC coating deposited on the plasma sprayed underlayer resulted in a total coating thickness of over 125 μm .
- A promising coating–substrate adhesion strength was obtained when using sintered–crushed hydroxyapatite powder, with a critical load of 69 N, reaching nearly 50% of standard plasma spray coating reference.
- A possible explanation for the high coating adhesion and the unique mixed (adhesive–cohesive) failure mode could be related to the high density of the powder particles.

More specific analyses could be conducted for a better understanding of the physico-chemical interactions between the raw powders and the substrate, as TEM or $\mu\text{-XRD}$ analysis, to evaluate the grain deformation at the nanoscale or local phase changes at the interface; however, cold spraying seems to be a valid alternative to high temperature technologies for the production of biocompatible coatings in the orthopaedic and biomedical fields.

Author Contributions: Conceptualization, G.B. and A.P.; methodology, G.B. and A.P.; software, J.A. and Y.B.; validation, G.B., J.A. and Y.B.; formal analysis, A.P.; investigation, A.P.; resources, G.B.; data curation, A.P. and J.A.; writing—original draft preparation, A.P.; writing—review and editing, G.B.; project administration, G.B.; funding acquisition, G.B. All authors have read and agreed to the published version of the manuscript.

Funding: This work is supported by the Agence Nationale de la Recherche of France under project named ARCHICAP (ANR-15-CE19-0021) and the Région Occitanie in France under project named REVAMITIC (CLE 2016).

Institutional Review Board Statement: Not applicable.

Informed Consent Statement: Not applicable.

Data Availability Statement: Not applicable.

Acknowledgments: We would like to thank Sergi Dosta and the CPT in Barcelona for the cold spray sessions and the support provided during the whole project.

Conflicts of Interest: The authors declare no conflict of interest.

References

1. Pisani, P.; Renna, M.D.; Conversano, F.; Casciaro, E.; Di Paola, M.; Quarta, E.; Muratore, M.; Casciaro, S.; Pisani, P.; Renna, M.D.; et al. Major Osteoporotic Fragility Fractures: Risk Factor Updates and Societal Impact. *World J. Orthop.* **2016**, *7*, 171–181. [[CrossRef](#)] [[PubMed](#)]
2. Xing, D.; Xu, Y.; Liu, Q.; Ke, Y.; Wang, B.; Li, Z.; Lin, J. Osteoarthritis and All-Cause Mortality in Worldwide Populations: Grading the Evidence from a Meta-Analysis. *Sci. Rep.* **2016**, *6*, 24393. [[CrossRef](#)] [[PubMed](#)]
3. Kurtz, S.M.; Ong, K.L.; Lau, E.; Widmer, M.; Maravic, M.; Gomez-Barrena, E.; de Fatima de Pina, M.; Manno, V.; Torre, M.; Walter, W.L.; et al. International Survey of Primary and Revision Total Knee Replacement. *Int. Orthop.* **2011**, *35*, 1783–1789. [[CrossRef](#)] [[PubMed](#)]
4. Bakhsheshi-Rad, H.R.; Hamzah, E.; Ismail, A.F.; Sharer, Z.; Abdul-Kadir, M.R.; Daroonparvar, M.; Saud, S.N.; Medraj, M. Synthesis and Corrosion Behavior of a Hybrid Bioceramic-Biopolymer Coating on Biodegradable Mg Alloy for Orthopaedic Implants. *J. Alloys Compd.* **2015**, *648*, 1067–1071. [[CrossRef](#)]
5. Chambard, M.; Marsan, O.; Charvillat, C.; Grossin, D.; Fort, P.; Rey, C.; Gitzhofer, F.; Bertrand, G. Effect of the Deposition Route on the Microstructure of Plasma-Sprayed Hydroxyapatite Coatings. *Surf. Coat. Technol.* **2019**, *371*, 68–77. [[CrossRef](#)]
6. Khokhlova, M.; Dykas, M.; Krishnan-Kutty, V.; Patra, A.; Venkatesan, T.; Prellier, W. Oxide Thin Films as Bioactive Coatings. *J. Phys. Condens. Matter* **2019**, *31*, 033001. [[CrossRef](#)]
7. Catauro, M.; Barrino, F.; Blanco, I.; Piccolella, S.; Pacifico, S. Use of the Sol-Gel Method for the Preparation of Coatings of Titanium Substrates with Hydroxyapatite for Biomedical Application. *Coatings* **2020**, *10*, 203. [[CrossRef](#)]
8. Mhaede, M.; Ahmed, A.; Wollmann, M.; Wagner, L. Evaluating the Effects of Hydroxyapatite Coating on the Corrosion Behavior of Severely Deformed 316Ti SS for Surgical Implants. *Mater. Sci. Eng. C* **2015**, *50*, 24–30. [[CrossRef](#)]
9. Goodman, S.B.; Yao, Z.; Keeney, M.; Yang, F. Biomaterials the Future of Biologic Coatings for Orthopaedic Implants. *Biomaterials* **2013**, *34*, 3174–3183. [[CrossRef](#)]
10. Bosco, R.; Van Den Beucken, J.; Leeuwenburgh, S.; Jansen, J. Surface Engineering for Bone Implants: A Trend from Passive to Active Surfaces. *Coatings* **2012**, *2*, 95–119. [[CrossRef](#)]
11. Zhang, B.G.X.; Myers, D.E.; Wallace, G.G.; Brandt, M. Bioactive Coatings for Orthopaedic Implants—Recent Trends in Development of Implant Coatings. *Int. J. Mol. Sci.* **2014**, *15*, 11878–11921. [[CrossRef](#)] [[PubMed](#)]
12. Søballe, K. Hydroxyapatite Ceramic Coating for Bone Implant Fixation. *Acta Orthop. Scand.* **1993**, *64*, 1–58. [[CrossRef](#)] [[PubMed](#)]
13. Abu-amer, Y.; Darwech, I.; Clohisy, J.C. Aseptic Loosening of Total Joint Replacements: Mechanisms Underlying Osteolysis and Potential Therapies. *Arthritis Res. Ther.* **2007**, *9*, S6. [[CrossRef](#)] [[PubMed](#)]
14. Cüneyt Tas, A. Synthesis of Biomimetic Ca-Hydroxyapatite Powders at 37 °C in Synthetic Body Fluids. *Biomaterials* **2000**, *21*, 1429–1438. [[CrossRef](#)]
15. Vandecandelaere, N.; Rey, C.; Drouet, C. Biomimetic Apatite-Based Biomaterials: On the Critical Impact of Synthesis and Post-Synthesis Parameters. *J. Mater. Sci. Mater. Med.* **2012**, *23*, 2593–2606. [[CrossRef](#)]
16. Tampieri, A.; Celotti, A.G.; Landi, A.E. From Biomimetic Apatites to Biologically Inspired Composites. *Anal. Bioanal. Chem.* **2005**, *381*, 568–576. [[CrossRef](#)]
17. Tampieri, A.; Celotti, G.; Landi, E.; Sandri, M.; Roveri, N.; Falini, G. Biologically Inspired Synthesis of Bone-like Composite: Self-Assembled Collagen Fibers/Hydroxyapatite Nanocrystals. *J. Biomed. Mater. Res. Part A* **2003**, *67A*, 618–625. [[CrossRef](#)]
18. Cazalbou, S.; Combes, C.; Eichert, D.; Rey, C.; Glimcher, M.J. Poorly Crystalline Apatites: Evolution and Maturation In Vitro and In Vivo. *J. Bone Miner. Metab.* **2004**, *22*, 310–317. [[CrossRef](#)]
19. Kafalak, A.; Kolodziejski, W. Complementary Information on Water and Hydroxyl Groups in Nanocrystalline Carbonated Hydroxyapatites from TGA, NMR and IR Measurements. *J. Mol. Struct.* **2011**, *990*, 263–270. [[CrossRef](#)]
20. Oyane, A.; Kakehata, M.; Sakamaki, I.; Pyatenko, A.; Yashiro, H.; Ito, A.; Torizuka, K. Biomimetic Apatite Coating on Yttria-Stabilized Tetragonal Zirconia Utilizing Femtosecond Laser Surface Processing. *Surf. Coat. Technol.* **2016**, *296*, 88–95. [[CrossRef](#)]
21. Li, P. Biomimetic Nano-Apatite Coating Capable of Promoting Bone Ingrowth. *J. Biomed. Mater. Res. Part A* **2003**, *66A*, 79–85. [[CrossRef](#)] [[PubMed](#)]
22. Davis, J.R. *Thermal Spray Technology*; ASM International: Almere, The Netherlands, 2004; ISBN 0871707950.

23. Moridi, A.; Guagliano, M.; Dao, M. Cold Spray Coating: Review of Material Systems and Future Perspectives. *Surf. Eng.* **2014**, *36*, 369–395. [[CrossRef](#)]
24. Sova, A.; Kosarev, V.F.; Papyrin, A.; Smurov, I. Effect of Ceramic Particle Velocity on Cold Spray Deposition of Metal-Ceramic Coatings. *J. Therm. Spray Technol.* **2011**, *20*, 285–291. [[CrossRef](#)]
25. Gardon, M.; Concustell, A.; Dosta, S.; Cinca, N.; Cano, I.G.; Guilemany, J.M. Improved Bonding Strength of Bioactive Cermet Cold Gas Spray Coatings. *Mater. Sci. Eng. C* **2014**, *45*, 117–121. [[CrossRef](#)]
26. Zhou, X.; Mohanty, P. Electrochemical Behavior of Cold Sprayed Hydroxyapatite/Titanium Composite in Hanks' Solution. *Electrochim. Acta* **2012**, *65*, 134–140. [[CrossRef](#)]
27. Irissou, E.; Legoux, J.; Arsenault, B.; Moreau, C. Investigation of Al-Al₂O₃ Cold Spray Coating Formation and Properties. *J. Therm. Spray Technol.* **2007**, *16*, 661–668. [[CrossRef](#)]
28. Siao, A.; Ang, M.; Berndt, C.C.; Cheang, P. Surface & Coatings Technology Deposition Effects of WC Particle Size on Cold Sprayed WC—Co Coatings. *Surf. Coat. Technol.* **2011**, *205*, 3260–3267. [[CrossRef](#)]
29. Vilardell, A.M.; Cinca, N.; Concustell, A.; Dosta, S.; Cano, I.G.; Guilemany, J.M. Cold Spray as an Emerging Technology for Biocompatible and Antibacterial Coatings: State of Art. *J. Mater. Sci.* **2015**, *50*, 4441–4462. [[CrossRef](#)]
30. Kergourlay, B.E.; Grossin, D.; Cinca, N.; Josse, C.; Dosta, S.; Bertrand, G.; Garcia, I.; Guilemany, J.M.; Rey, C.; Rey, P.C. First Cold Spraying of Carbonated Biomimetic Nanocrystalline Apatite on Ti6Al4V: Physical—Chemical, Microstructural, and Preliminary Mechanical Characterizations. *Adv. Eng. Mater.* **2016**, *18*, 496–500. [[CrossRef](#)]
31. Moreau, D.; Borit, F.; Corté, L.; Guipont, V. Cold Spray Coating of Submicronic Ceramic Particles on Poly(Vinyl Alcohol) in Dry and Hydrogel States. *J. Therm. Spray Technol.* **2017**, *26*, 958–969. [[CrossRef](#)]
32. Yao, H.L.; Yang, G.J. *Cold Spray Processing for Micro-Nano Ceramic Coatings*; Elsevier Inc.: Amsterdam, The Netherlands, 2019; ISBN 9780128138700.
33. Wang, L.S.; Zhou, H.F.; Zhang, K.J.; Wang, Y.Y.; Li, C.X.; Luo, X.T.; Yang, G.J.; Li, C.J. Effect of the Powder Particle Structure and Substrate Hardness during Vacuum Cold Spraying of Al₂O₃. *Ceram. Int.* **2017**, *43*, 4390–4398. [[CrossRef](#)]
34. Helfritsch, D. *A Model Study of Powder Particle Size Effects in Cold Spray Deposition*; U.S. Army Research Laboratory, Aberdeen Proving Ground: Aberdeen, MD, USA, 2014.
35. Nouri, A.; Sola, A. Powder Morphology in Thermal Spraying. *J. Adv. Manuf. Process.* **2019**, *1*, e10020. [[CrossRef](#)]
36. Fauchais, P.; Montavon, G.; Bertrand, G. From Powders to Thermally Sprayed Coatings. *J. Therm. Spray Technol.* **2010**, *19*, 56–80. [[CrossRef](#)]
37. Jeandin, M.; Rolland, G.; Descurninges, L.L.; Berger, M.H. Which Powders for Cold Spray? *Surf. Eng.* **2014**, *30*, 291–298. [[CrossRef](#)]
38. Lee, D.W.; Kim, H.J.; Kim, Y.N.; Jeon, M.S.; Nam, S.M. Substrate Hardness Dependency on Properties of Al₂O₃ Thick Films Grown by Aerosol Deposition. *Surf. Coat. Technol.* **2012**, *209*, 160–168. [[CrossRef](#)]
39. Demnati, I.; Grossin, D.; Combes, C.; Rey, C. Plasma-Sprayed Apatite Coatings: Review of Physical-Chemical Characteristics and Their Biological Consequences. *J. Med. Biol. Eng.* **2014**, *34*, 1–7. [[CrossRef](#)]
40. Sun, L.; Berndt, C.C.; Gross, K.A.; Kucuk, A. Material Fundamentals and Clinical Performance of Plasma-Sprayed Hydroxyapatite Coatings: A Review. *J. Biomed. Mater. Res.* **2001**, *58*, 570–592. [[CrossRef](#)]
41. Tsui, Y.C.; Doyle, C.; Clyne, T.W. Plasma Sprayed Hydroxyapatite Coatings on Titanium Substrates Part 1: Mechanical Properties and Residual Stress Levels. *Biomaterials* **2015**, *19*, 2015–2029. [[CrossRef](#)]
42. Villa, M.; Dosta, S.; Fernández, J.; Guilemany, J.M. La Proyección Fría (CGs): Una Alternativa a Las Tecnologías Convencionales de Deposición. *Rev. Metal.* **2012**, *48*, 175–191. [[CrossRef](#)]
43. Kergourlay, E. Apatites Nanocrystallines Biomimétiques Carbonatées Pour Applications Médicales: De La Synthèse Des Poudres Aux Revêtements Par Projection Dynamique à Froid (Cold Spray). Ph.D. Thesis, Institut National Polytechnique de Toulouse, Toulouse, Paris, France, 2016.
44. Emery, E.; Oliver, J.; Pugsley, T.; Sharma, J.; Zhou, J. Flowability of Moist Pharmaceutical Powders. *Powder Technol.* **2009**, *189*, 409–415. [[CrossRef](#)]
45. Attia, U.M.; Fones, A.; Trepleton, R.; Hamilton, H.; Davies, S.; Wimpenny, D. HIPing of Pd-Doped Titanium Components: A Study of Mechanical and Corrosion Properties Properties. In Proceedings of the 11th International Conference of Hot Isostatic Pressing, Stockholm, Sweden, 9–13 June 2014.
46. Reddy, R.S.; Ramachandra, C.T.; Hiregoudar, S.; Nidoni, U.; Ram, J.; Kammar, M. Influence of Processing Conditions on Functional and Reconstitution Properties of Milk Powder Made from Osmanabadi Goat Milk by Spray Drying. *Small Rumin. Res.* **2014**, *119*, 130–137. [[CrossRef](#)]
47. Cullity, B.; Stock, S. *Elements of X-ray Diffraction*, 3rd ed.; Prentice-Hall Inc.: Hoboken, NJ, USA, 2001.
48. Ren, F.; Leng, Y. Carbonated Apatite, Type-A or Type-B? *Key Eng. Mater.* **2012**, *493*, 293–297. [[CrossRef](#)]
49. Kudo, Y.; Yasuda, M.; Matsusaka, S. Effect of Particle Size Distribution on Flowability of Granulated Lactose. *Adv. Powder Technol.* **2020**, *31*, 121–127. [[CrossRef](#)]
50. Silva, A.P.; Pinto, D.G.; Segadães, A.M.; Devezas, T.C. Designing Particle Sizing and Packing for Flowability and Sintered Mechanical Strength. *J. Eur. Ceram. Soc.* **2010**, *30*, 2955–2962. [[CrossRef](#)]
51. Liu, L.X.; Marziano, I.; Bentham, A.C.; Litster, J.D.; White, E.T.; Howes, T. Effect of Particle Properties on the Flowability of Ibuprofen Powders. *Int. J. Pharm.* **2008**, *362*, 109–117. [[CrossRef](#)]

52. Hanft, D.; Exner, J.; Schubert, M.; Stöcker, T.; Fuierer, P.; Moos, R. An Overview of the Aerosol Deposition Method: Process Fundamentals and New Trends in Materials Applications. *J. Ceram. Sci. Technol.* **2015**, *6*, 147–181. [[CrossRef](#)]
53. Winnicki, M. Advanced Functional Metal-Ceramic and Ceramic Coatings Deposited by Low-Pressure Cold Spraying: A Review. *Coatings* **2021**, *11*, 1044. [[CrossRef](#)]
54. Mohseni, E.; Zalnezhad, E.; Bushroa, A.R. Comparative Investigation on the Adhesion of Hydroxyapatite Coating on Ti-6Al-4V Implant: A Review Paper. *Int. J. Adhes. Adhes.* **2014**, *48*, 238–257. [[CrossRef](#)]
55. Fernández-Pradas, J.M.; Clèries, L.; Martínez, E.; Sardin, G.; Esteve, J.; Morenza, J.L. Influence of Thickness on the Properties of Hydroxyapatite Coatings Deposited by KrF Laser Ablation. *Biomaterials* **2001**, *22*, 2171–2175. [[CrossRef](#)]
56. Singh, H.; Sidhu, T.S.; Kalsi, S.B.S. Cold Spray Technology: Future of Coating Deposition Processes. *Frat. Integrita Strutt.* **2012**, *22*, 69–84. [[CrossRef](#)]
57. Jodoin, B.; Raletz, F.; Vardelle, M. Cold Spray Modeling and Validation Using an Optical Diagnostic Method. *Surf. Coat. Technol.* **2006**, *200*, 4424–4432. [[CrossRef](#)]
58. Goyal, T.; Walia, R.S.; Sidhu, T.S. Effect of Parameters on Coating Density for Cold Spray Process. *Mater. Manuf. Process.* **2012**, *27*, 193–200. [[CrossRef](#)]
59. Schmidt, T.; Assadi, H.; Gärtner, F.; Richter, H.; Stoltenhoff, T.; Kreye, H.; Klassen, T. From Particle Acceleration to Impact and Bonding in Cold Spraying. *J. Therm. Spray Technol.* **2009**, *18*, 794–808. [[CrossRef](#)]